Applied Surface Science Advances 6 (2021) 100168

Contents lists available at ScienceDirect

Applied Surface Science Advances

journal homepage: www.sciencedirect.com/journal/applied-surface-science-advances

Enhancing rate capability of graphite anodes for lithium-ion batteries by pore-structuring

Daeun Jang[a,1], Seokho Suh[a,1], Hocheol Yoon[a], Jihun Kim[b], Hyunsu Kim[a], Juyeon Baek[a], Hyeong-Jin Kim[a,*]

[a] Graduate School of Energy Convergence, Institute of Integrated Technology, Gwangju Institute of Science and Technology, 123 Cheomdangwagi-ro, Buk-gu, Gwangju, 61005, South Korea

[b] Gwangju Bio/Energy R&D Center, Korea Institute of Energy Research (KIER), 270-25 Samso-ro, Buk-gu, Gwangju, 61003, South Korea

ARTICLE INFO

Keywords:
Lithium-ion batteries
Fast charging
Graphite anodes
Pore-structuring
Ionic diffusion

ABSTRACT

For the development of high-performance lithium-ion batteries (LIBs), numerous studies on 3-dimensionalized electrode structures have been conducted to improve the ionic diffusion, rate performance, and electrolyte wetting ability. Due to the decrease in ionic polarization, structured electrodes show much higher capacity retention compared to typical electrodes, especially at high current rates. In this study, pore-structured graphite (Gr) electrodes were synthesized using pore-formation agent particles (polytetrafluoroethylene (PTFE)), which possess a unique thermal unzipping property. After the heat treatment, the PTFE particles were depolymerized to form micro-sized pores. The effect of the 3-dimensionalized electrode structure on the electrochemical properties was investigated in detail. As a result, it was observed that the rate capability and cycle life of pore-structured Gr electrodes enhanced owing to their improved physical properties, such as wetting ability and shortened ionic diffusion pathways. Because our approach does not require changes in the existing electrode chemistry and slurry process, it is one of the most cost-effective and applicable ways to improve fast charging capability.

1. Introduction

The demand for lithium-ion batteries (LIBs), which possess excellent characteristics such as high energy density, high power density, and long cycle life, has been steadily increasing with the increase in the use of portable electronic devices and electric vehicles (EVs) [1–3]. In particular, for EV applications, fast charging capability is a critical issue that can reduce the charging time from hours to minutes [4–6].

To keep up with the demand for high-performance LIBs, many studies have been conducted on the optimization of the electrode structure. The migration of Li^+ ions in highly tortuous electrode structures and thick electrodes is difficult owing to inefficient transport [7]. Furthermore, tortuous electrode structures are accompanied with concentration polarization. Consequently, the deeper side of the electrodes shows less reaction with Li^+ ions compared to the electrode surface, which exhibits poor capacity retention at high current densities [8]. In addition, heterogeneous reactions in the electrode thickness direction could lead to Li plating and capacity fading [9–10].

To improve Li^+ ion transport limitations in the electrode, an electrode structure design with a facile Li^+ ion supply is a promising approach to improve the performance of LIBs [11–15]. Several approaches have been conducted to control the electrode morphology to enhance the diffusion rate of Li^+ ions. For example, Pfleging et al. conducted laser treatment on post-calendered electrodes to obtain a 3D microstructure called the micro-grooves [16]. The specific discharge capacity of the laser-structured electrodes improved significantly at a current rate of 1 C, resulting from the acceleration of electrolyte wetting in the electrodes. However, because laser structuring is inevitably accompanied with a slight loss of active material, it is preferable to minimize the electrode ablation [17]. Chen et al. improved the electrochemical performance of graphite (Gr) anodes using laser treatment while minimizing the electrode loss [18]. They produced 3D electrode architectures with arrays of vertical pore channels through the electrode thickness, resulting in rapid Li^+ ion transport. Consequently, the laser-patterned graphite electrode showed cycle ability greater than 97% and capacity retention greater than 93% after 100 cycles at current

---

[*] Corresponding author.
E-mail address: hjkimc@gist.ac.kr (H.-J. Kim).
[1] Co-first authors with equal contribution

https://doi.org/10.1016/j.apsadv.2021.100168
Received 7 June 2021; Received in revised form 17 August 2021; Accepted 14 September 2021

rates of 4C and 6C, respectively. Freeze casting is another method for fabricating 3D electrode structures. Dang et al. created a low-tortuous structure using the freeze-drying of slurries cast to fabricate the graphite electrodes. The low-tortuous structure improved the electrolyte-wetting ability and showed superior capacity retention and rate capability, which accounted for the enhanced ionic transport [19]. Chen et al. developed low-tortuosity carbon frameworks for facile Li^+ ion paths. The 3D electrodes exhibited high ionic and electronic properties. Dang and Chen showed a new electrode structure method that effectively transported Li^+ ions by lowering the tortuosity [20]. Pore-structuring, which uses thermally unzipped particles, has been reported as an effective way to obtain micro-structured electrodes and improve the performance of LIBs without capacity loss [21–23]. Choi et al. used polymethyl methacrylate (PMMA) as a pore-forming agent for Si-based electrodes. The porous architecture contributes to the development of cycle ability. Capacity retention of 62% was achieved after 100 cycles at a current rate of 0.5 C, whereas a typical Si electrode retained 39% capacity [24]. Lui et al. fabricated 3-dimensional ordered macroporous (3DOM) TiO_2 electrodes with highly enhanced ionic transfer. This electrode shows outstanding high-rate capability and provides a capacity of 174 mAh g^{-1} at a current rate of 2 A g^{-1}, which is 2.6 times greater than that of the original electrode (67 mAh g^{-1}) [25].

In this study, we conducted a physico-electrochemical characterization of pore-structured graphite electrodes. Polytetrafluoroethylene (PTFE) was used as a pore-formation additive due to its chemical stability and thermal properties of unzipping [26–28]. To the best of our knowledge, PTFE has been widely used as a pore agent in fuel cells and capacitors; however, few studies have adopted it for LIBs despite its excellent chemical stability and insolubility in almost all solvents. Poly (amic acid) (PAA) was used as a binder because its mechanical properties are improved by thermal treatment, whereas typical binders generally become brittle [29]. For the fabrication of pore-structured electrodes, the post-calendered electrodes consisting of Gr, conductive carbon, PAA binder, and PTFE (denoted as GCPP) were heat-treated at 600 °C for 1 h in an argon gas atmosphere. As a result, the ionic resistance in the structured electrodes was significantly reduced compared to the typical Gr electrodes, showing a significantly improved rate and cycle performance. Our approach is believed to be highly applicable to commercial LIBs as it does not require changes to the current slurry-casting process and expensive equipment for fabrication [30].

2. Experimental section

2.1. Sample preparation

In this study, we analyzed the cell performance of typical Gr electrodes and pore-structured Gr electrodes. The fabrication process of structured Gr electrodes is illustrated in Fig. 1. For the sample preparation, Gr, super C65 (MTI Korea, 99.8% purity) as a conductive carbon, PAA binder (PNS Technology), and PTFE (35 μm, Sigma-Aldrich) dissolved in N-methyl-2-pyrrolidone (NMP, 99.5% purity, Aldrich) solvent were homogeneously mixed using a planetary ball mill (PM100, Retsch Technology, Germany) with a rotation speed of 200 rpm for 30 min under an argon atmosphere. The weight ratio of each component (Gr powder, super C, PAA binder, PTFE) was 90:2:8:40, respectively. The thoroughly mixed slurry was coated on the Cu foil (thickness = 20 μm) with a doctor-blade. Thereafter, it was dried at 80 °C in the air for 20 min and then vacuum dried for 12 h. The dried electrode was uniformly calendared to have a porosity of 30% using a manual rolling press machine (TOB new energy, China). Next, the as-prepared GCPP electrodes were heated in the following process. First, they were annealed under argon flow from room temperature to 200 °C at a heating rate of 10 °C min^{-1}. Second, they were continuously heated to 600 °C at a low heating rate of 2 °C min^{-1} to prevent the formation of cracks in electrodes. Finally, the heating temperature was maintained at 600 °C for 1 h to depolymerize the PTFE in GCPP electrodes. As a result, the pore-former additive was decomposed to have a highly porous morphology: the porosity of pore-structured Gr electrodes is about 50%. For comparison, typical Gr electrodes were prepared with Gr, super C, and polyvinylidene fluoride (PVDF) binder in a 90:2:8 wt ratio: herein, the loading level of Gr active material is the same in typical and GCPP electrodes (8.5 mg cm^{-2}). For the coin-type full cells, typical cathodes were prepared with $LiNi_{0.8}Mn_{0.1}Co_{0.1}O_2$ (L&F, Korea), super C, and PVDF binder in a 90:4:6 wt ratio. We set the porosity of each electrode to 30% by calendering. The electrode porosity is defined as follows:

$$Porosity\ (\%) = \frac{V - W\left\{\frac{C_1}{\rho_1} + \frac{C_2}{\rho_2} + \frac{C_3}{\rho_3}\right\}}{V} \times 100 \qquad (1)$$

where V is the volume of the electrode composite, C is the proportion of each component in the electrode, W is the weight of electrode composite

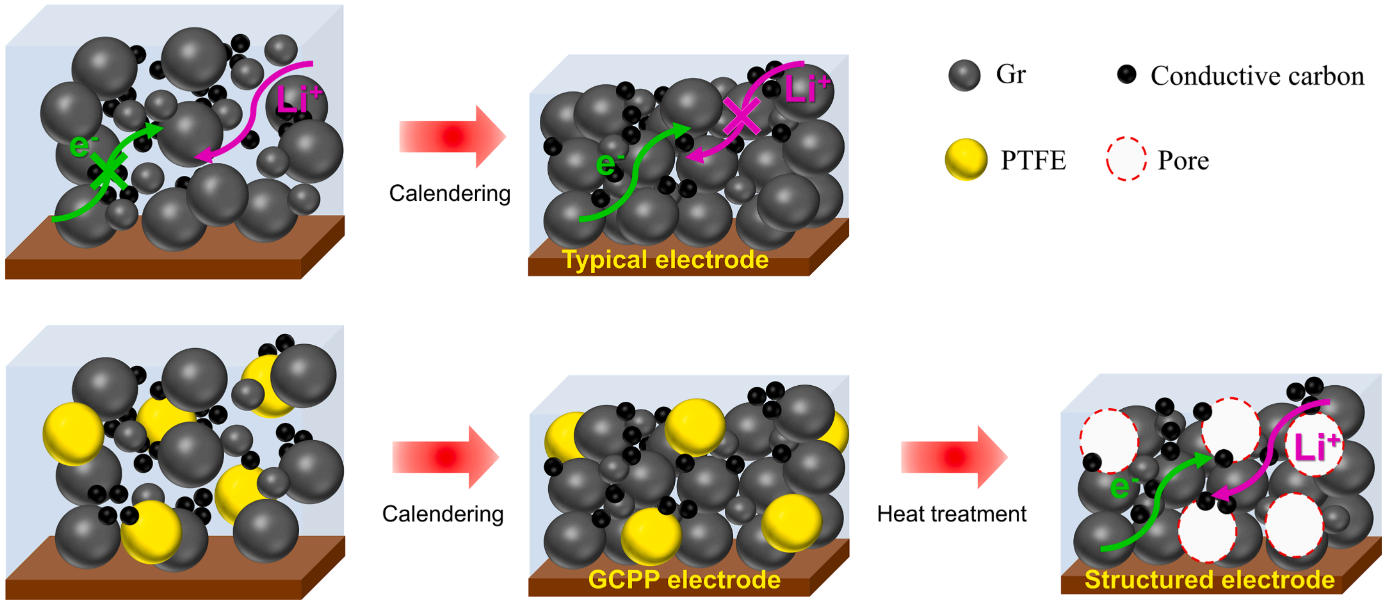

Fig. 1. Schematic illustration of typical Gr and pore-structured Gr electrodes, showing the trade-off between electrical and ionic conductivity in the typical electrode and improved ionic conductivity in the structured electrode.

per area, and ρ is the true density of each component.

2.2. Material characterization

The morphology and composition of the samples were investigated by scanning electron microscopy (SEM, Hitachi S-4700) and high-resolution transmission electron microscopy (HRTEM, JEM-2100F). X-ray photoelectron spectroscopy (XPS, MultiLab 2000) was employed to analyze the chemical composition and bonding configuration of the composites. For XPS measurements, a micro-focused monochromated Al Kα X-ray source was used under a vacuum of 5×10^{-9} mbar, and the analyzed region was 0.4 mm x 0.4 mm. Fourier-transform infrared (FTIR) spectroscopy was conducted to confirm the structure of the PAA binder before and after heat treatment. FTIR spectra were collected using a Vetex70v FTIR spectrometer at room temperature in the range of 650–4000 cm^{-1} with attenuated total reflectance (ATR) mode. To analyze the wetting characteristics of typical and structured Gr electrodes, contact angle measurements of a DI water droplet on electrodes were executed. Thermogravimetric analysis (TGA, TGA-50, SHIMADZU) was applied to investigate the decomposition temperature of PTFE. It was investigated under N_2 atmosphere at a heating rate of 5 °C min^{-1} from 25 °C to 600 °C. The electrode surface of samples was investigated by atomic force microscope (AFM, XE-100, Park systems). AFM measurement scale is 80 µm × 80 µm on each sample at a scan rate of 0.1 Hz. The surface area was calculated using the XEI program. Raman spectroscopy (Horiba, Optron, LabRAM HR Evolution) was performed using a 532 nm laser at 1.3 mW.

2.3. Electrochemical measurement

For electrochemical measurement, all working electrodes were punched into discs with a diameter of 10 mm: loading mass of Gr and $LiNi_{0.8}Mn_{0.1}Co_{0.1}O_2$ (NMC811, L&F materials) in each electrode was approximately 8.5 mg cm^{-2} and 14 mg cm^{-2}. The electrodes were assembled into CR2032 coin cell in an argon-filled glove box with O_2 and H_2O contents of less than 0.6 ppm. A polypropylene membrane (Celgard 2400, thickness of 20 µm, diameter of 19 mm) was used as the separator. The electrolyte contained 1 M $LiPF_6$ in ethylene carbonate (EC) / diethyl carbonate (DEC) (1:1, v/v). After assembly, cells were stabilized for 12 h at room temperature for thorough wetting.

To evaluate electrochemical performance, galvanostatic charge-discharge cycling tests were conducted on Gr-NMC811 full cell in the voltage range of 2.5–4.3 V, using a battery cycler (WBCS 3000, Wonatech, Korea). In structured Gr/NMC811 full cells, the n/p ratios were set to around 0.9 to compensate for the capacity loss originating from SEI (Solid Electrolyte Interphase) formation [31–32], whereas it was 1.0 in typical Gr electrodes. For forming a stable SEI layer, Gr/NMC811 full cells were pre-cycled at a low current rate of 0.1C in the initial 5 cycles. Then, rate capability tests were conducted at variant charging current rates from 1C to 3C with a fixed discharging current rate at 0.5C. Cycling tests were implemented at the charging rate of 2C and discharging rate of 0.5C. Specific capacities and current densities were based on the mass of Gr active material ($1\text{C} = 372\ \text{mA g}^{-1}{}_{\text{Gr}}$).

Electrochemical impedance spectroscopy (EIS) was conducted on typical and structured Gr electrodes to analyze ionic resistance (R_{ion}), associated with diffusion resistance as Li^+ ions pass through pores in electrodes. In particular, we assembled pristine symmetric cells, which were composed of two same electrodes, to investigate the intrinsic impedance characteristics of each electrode. All EIS measurements were carried out at a voltage amplitude of 10 mV in a frequency range from 200 kHz to 100 mHz using a potentiostat (VSP, Biologic, France). Nyquist plot fitting was conducted using the Z-Fit program (Biologic) which can calculate the internal resistance value in the electrode. To identify electrode resistance, we considered ohmic resistance, electronic resistance (contact resistance), constant phase element (CPE), and modified restricted linear diffusion.

To compare the electrochemically active surface area (ECSA) of Gr electrodes, cyclic voltammetry (CV) test was employed using non-lithium intercalating electrolyte, which is 0.1 M tetrabutylammonium perchlorate ($TBAClO_4$, Sigma- Aldrich, USA, >99%) in EC/DMC (1:1, v/v) to prevent a faradaic current. The CV measurement was performed at open circuit potential (OCP) to identify the electrode capacitive currents. The potential range was set to −50 to 50 mV (vs. saturated calomel electrode, SCE) at scan rates from 2 mV s^{-1} to 8 mV s^{-1}. The specific capacitance of Gr electrodes was calculated as follows [33–34].

$$C_{sp} = \frac{I_c - I_d}{s \cdot m} \tag{2}$$

Where C_{sp}, is the specific capacitance (F g^{-1}), I_c and I_d are cathodic and anodic current density (mA g^{-1}), s is the scan rate (mV s^{-1}), and m is the active material mass of an electrode (g).

2.4. Tortuosity measurement

Tortuosity of the electrode can be calculated through the R_{ion} value obtained through the symmetric cell EIS. Tortuosity (τ) can be calculated as follows [19]

$$\tau = \frac{R_{ion} \cdot A \cdot k \cdot \varepsilon}{2d} \tag{3}$$

where A, d, and ε are the surface area, thickness, and porosity of the electrode, respectively; κ (8.17 mS cm^{-1}) is the conductivity of the electrolyte. Tortuosity values were divided by two in order to only account for one of the two electrodes.

3. Results and discussion

3.1. Materials characterization

Fig. 1 schematic illustration shows the ionic diffusion limitation in typical electrodes, and the improved diffusion pathway in structured electrodes. In general, the calendering process is essential for Gr anodes to generate conductive networks in electrodes [35–36]. However, several closed pores are formed after calendaring, resulting in poor electrolyte wetting ability and Li^+ ion transport [37]. In particular, in high current rates, limiting ionic pathways in calendered electrodes causes low capacity retention originating from ionic polarization. In addition, Li^+ ion could be plated on the Gr anode during fast charging, which incurs severe capacity decay and safety issues. In structured electrodes, abundant pore networks facilitate ionic diffusion migration and prevent Li plating through rapid Li^+ ion flux.

Figure S1a shows a digital image of Gr, conductive carbon, and PTFE particles in equal proportions in a GCPP electrode. The apparent volume of the PTFE particles seems approximately same as that of graphite; therefore, significant pores are expected to form in the structured electrode. Figure S1(b–d) show the SEM images of Gr, carbon, and PTFE; the average particle sizes were ~20 µm, ~55 nm, and ~35 µm, respectively. The irregular PTFE particle sizes result in a non-uniform pore size distribution of the structured Gr electrode, as shown in Figure S1d. Because graphite particles are densely covered with nano-sized conductive carbons and binders, the surface of a typical electrode seems impenetrable, as shown in Fig. 2(a–c). The PTFE particles were embedded with Gr particles in a GCPP electrode, as shown in Fig. 2(d–f). Figure S1d shows an SEM image of the elliptical-shaped PTFE particles. Due to the high ductility of PTFE particles, they were transformed into a flat shape through calendering as the particles were not crushed by pressing. After heat treatment, the PTFE particles were thermally unzipped and micro-sized pores were developed, as shown in Fig. 2(g–i).

The increased pore sizes in structured Gr electrodes were expected to provide electrolyte-penetrating routes and ionic transport pathways. The typical electrode exhibited a dense electrode structure with several closed pores, which disturbed the electrolyte wetting and Li^+ ion

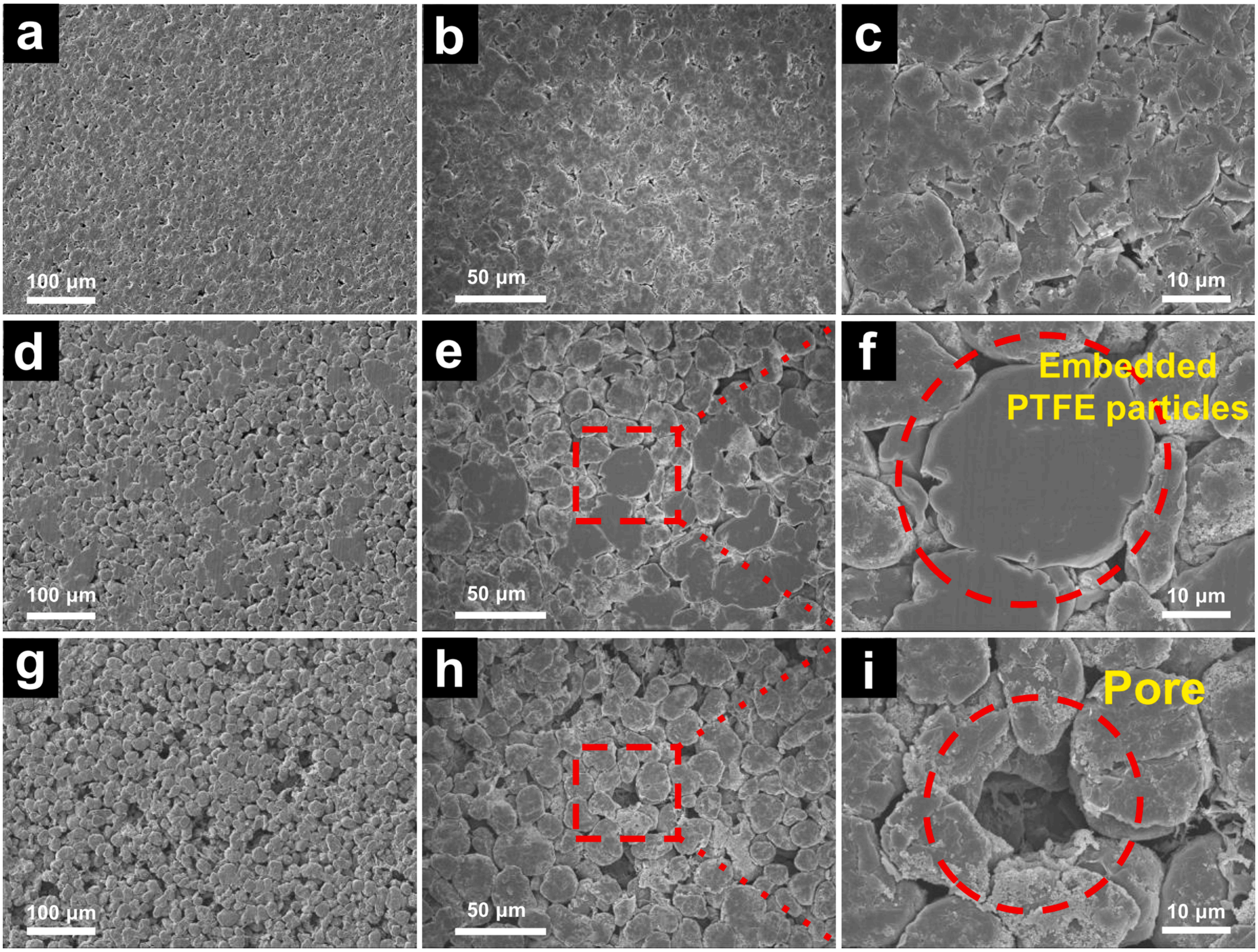

Fig. 2. Top-down SEM images of the (a–c) typical Gr, (d–f) GCPP, and (g–i) structured Gr electrode.

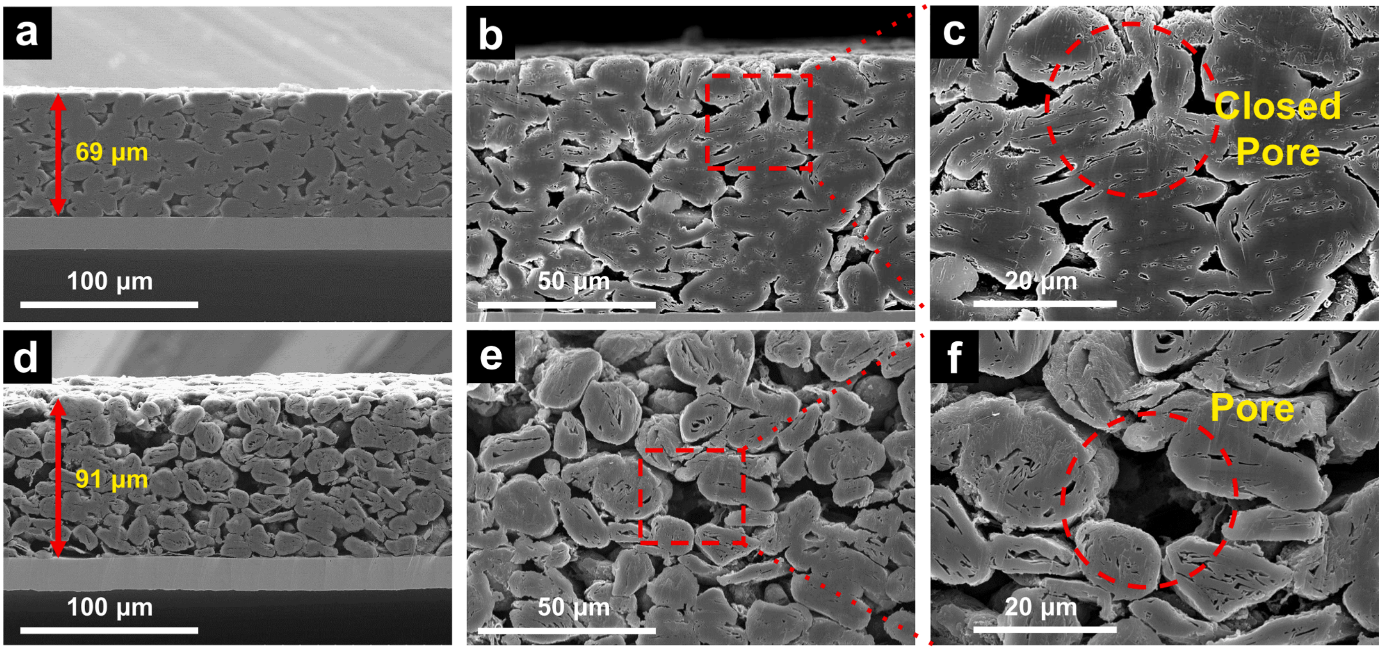

Fig. 3. Cross-sectional SEM images of the (a–c) typical Gr and (d–f) structured Gr electrodes.

diffusion in Fig. 3(a–c). However, the pore-structured Gr electrode revealed a lot of micro-sized pores, which were expected to enhance the wetting ability and ionic diffusion rate.

Contact angle measurements were employed to investigate the wetting ability of typical and structured Gr electrodes, as shown in Fig. 4. For a typical electrode, the initial contact angle of a DI water solvent drop was 84°, compared to a structured electrode, which was comparatively 1.16 times lower (72°). In addition, further wetting of the structured electrode was faster than that of a typical electrode, as shown in Fig. 2c. After allowing the wetting of a structured electrode for additional 10 min, the contact angle became twice (14°) than that of a typical electrode (7°).

For further analysis of the electrode surface morphology, AFM measurements were conducted on Gr electrodes, as shown in Figure S3. The roughness average (Ra) of a structured Gr electrode was 0.496 µm, whereas a typical Gr electrode exhibited a roughness of 0.321 µm, showing enhanced electrode surface roughness. The changes in physical properties due to pore structuring are believed to improve ionic diffusion, which is the rate-determining step at high current rates.

The surface chemistry of GCPP electrodes before and after the heat treatment was investigated using XPS measurements to confirm the removal of PTFE particles during thermal treatment, as shown in Fig. 5 (a–b). As shown in Fig. 5a, for a GCPP electrode, the XPS spectrum of C 1 s can be divided into two peaks. One peak is at 285 eV, which is associated with C—C (or $C = C$) bonds in Gr, PAA binder, and conductive carbon [38–40], and the other is at 292 eV, which corresponds to the C-F bond in PTFE [41]. After annealing, the peak at 292 eV disappeared, indicating that the PTFE particles were successfully eliminated. In the F 1 s spectrum, in Fig. 5b, a C-F bond-related peak at 689 eV vanished after heat treatment [41].

TGA measurements were performed to investigate the thermal behavior of PTFE powders. As shown in Fig. 5c, PTFE thermally decomposes at temperatures above 450 °C, showing that heating the GCPP electrode at 600 °C for 1 h is considered a sufficient condition to eliminate all the PTFE particles. In conclusion, the removal of PTFE powders during thermal treatment was demonstrated using XPS and TGA measurements, which were consistent with the SEM images of the structured Gr electrode shown in Fig. 2(g–i).

The FT-IR spectra of the PAA binder before and after the heat treatment are shown in Fig. 5d. The typical peaks of PAA were observed at 1720 cm^{-1}, and 1650 cm^{-1} related to $C = O$ stretching in the acid and amide functional groups [42]. In addition, the N—H bending peak of the amide group was observed at 1502 cm^{-1} [43]. After heat treatment of PAA, the characteristic amide peaks disappeared, while several new peaks corresponding to polyimide (PI) appeared. The peaks at 1776 cm^{-1} and 1720 cm^{-1} correspond to the $C = O$ asymmetric and symmetric vibrations of the imide group in PI, respectively [42,44]. The C—N stretching in the imide ring was observed at approximately 1370 cm^{-1} [45]. In general, the heat treatment of the electrode has a disadvantage as the binder materials are pyrolyzed at high temperatures (typically above 300 °C), and the binding ability to fix the active materials to a current collector weakens, resulting in cracks and deterioration of the electrode structure [46–47]. However, as the PI binder is known to possess remarkable mechanical properties and thermal stability [48–49], it is plausible that structural integrity of the structured Gr electrode was maintained without structural degradation during the heating process, as can be seen in Figs. 3 and 4.

Raman spectroscopy was adopted to compare the crystallinity of pristine and heat-treated graphite particles (600 °C for 1 h), as shown in Figure S4. The D band at 1355 cm^{-1} and G band at 1583 cm^{-1} correspond to the disordered sp^2 hybridized carbon and the E_{2g} symmetry of the sp^2 hybridized carbon, respectively. The intensity ratio values of I_D/I_G of the Gr particles were similar, showing no significant changes in crystallinity during heat treatment.

3.2. Electrochemical characterization

Fig. 6 shows the EIS results of typical and structured Gr electrodes used to analyze the internal resistance. The data obtained using an equivalent circuit model in Fig. 6a are well-fitted with the experimental data. In the high-frequency range, a semicircle is associated with electronic resistance, which is related to the contact resistance between the particles and the electrode material and current collector [50]. In the mid to low frequency range, 45° slope is related to the Li^+ ion diffusion resistance through the electrolyte-filled pores in the electrodes [51]. The contact resistance is almost identical to the typical (0.5 Ωcm^2) and structured (0.8 Ωcm^2) Gr electrodes. In contrast, at mid to low frequency, a structured Gr electrode shows two times lower Rion compared to a typical Gr electrode (37.6 → 17.7 Ω cm^2). This demonstrates improved ionic diffusion rate through the electrolyte-filled pores in electrodes. As indicated in Fig. 2(a–c), because the graphite particles were densely packed among the conductive carbons and binders, it is plausible that such materials interrupted the Li^+ ion diffusion [52].

To investigate the 3D electrode structural effects on the ionic diffusion pathways, the tortuosity was calculated based on Eq. (2) to measure the effective Li^+ ion diffusion length in typical and structured Gr electrodes. In general, 3D electrodes exhibit low tortuosity values, providing low-tortuous pathways for ionic transport [53–54]. As a result, the tortuosity values for typical and structured Gr electrodes were 6.67 and 3.98, respectively, showing a reduction in the apparent ionic diffusion length by 40% in Table 1. This is owing to the numerous micro-sized pores in the structured Gr electrode, which improved the ionic diffusion network and electrolyte wetting ability. The improved physical properties of the 3D electrode are expected to contribute to the enhancement of rate capability, especially at high current rates [55–56].

The state of charge (SOC) was set to SOC50 for each Gr electrode to analyze the SEI resistance (Rsei) and charge transfer resistance (Rct). As a result, the Rct of a structured Gr electrode reduced from 19.8 Ω cm^2 to 3.6 Ω cm^2, whereas the Rsei increased from 5.5 Ω cm^2 to 10.4 Ω cm^2, as shown in Figure S2. This result is ascribed to the enlarged electroactive

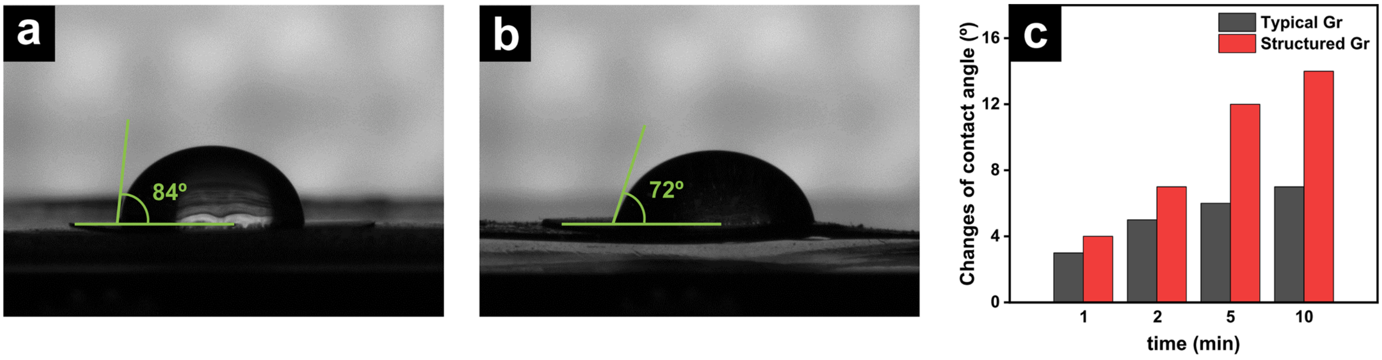

Fig. 4. Contact angle of a DI water solvent drop on the (a) typical Gr, (b) pore-structured Gr electrodes, and (c) changes in the contact angles over wetting time.

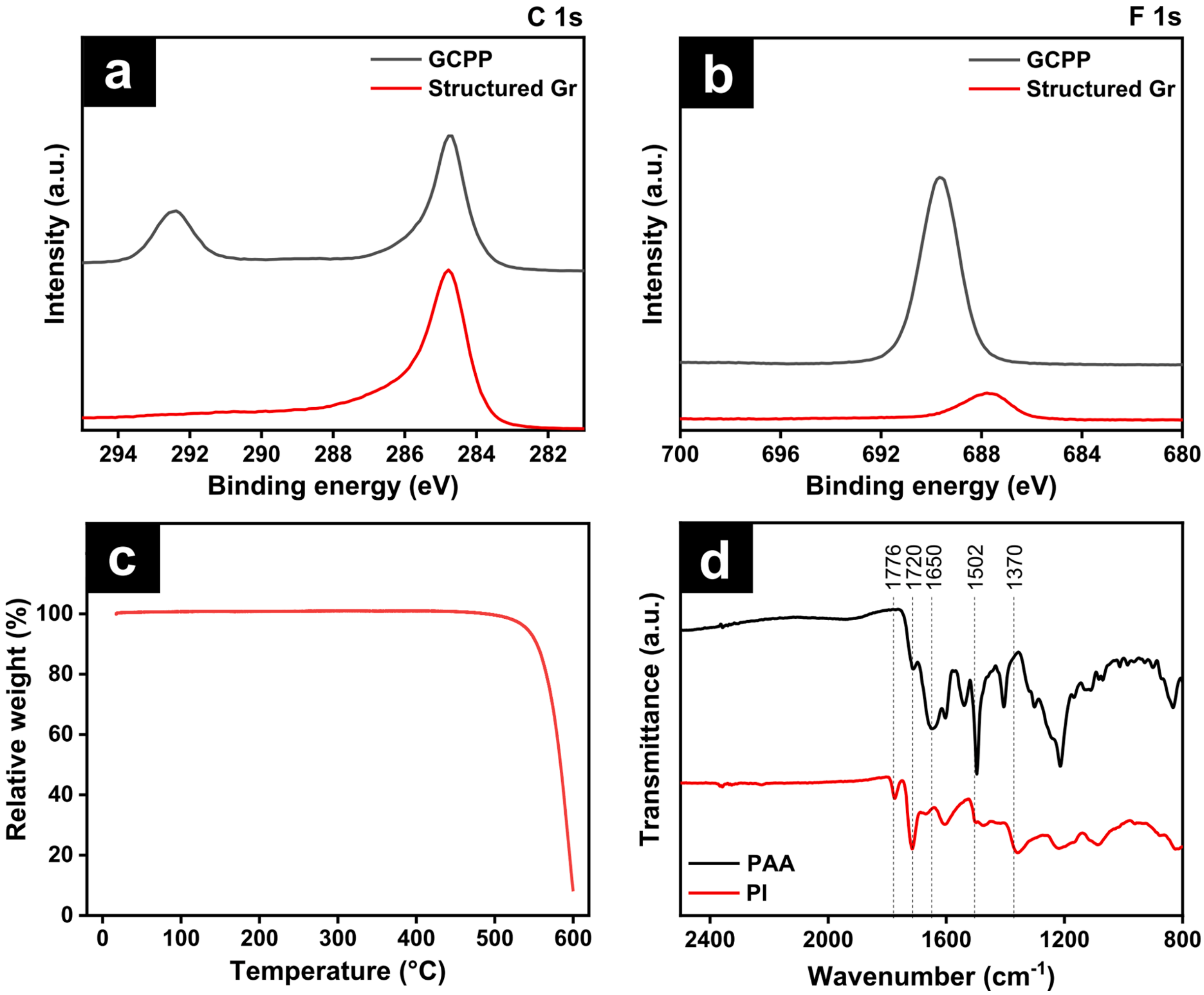

Fig. 5. XPS spectra of (a) C 1 s, (b) F 1 s before and after the heat treatment on GCPP electrode, (c) TGA curve of PTFE, and (d) FTIR spectra of pristine and heat-treated PAA binder.

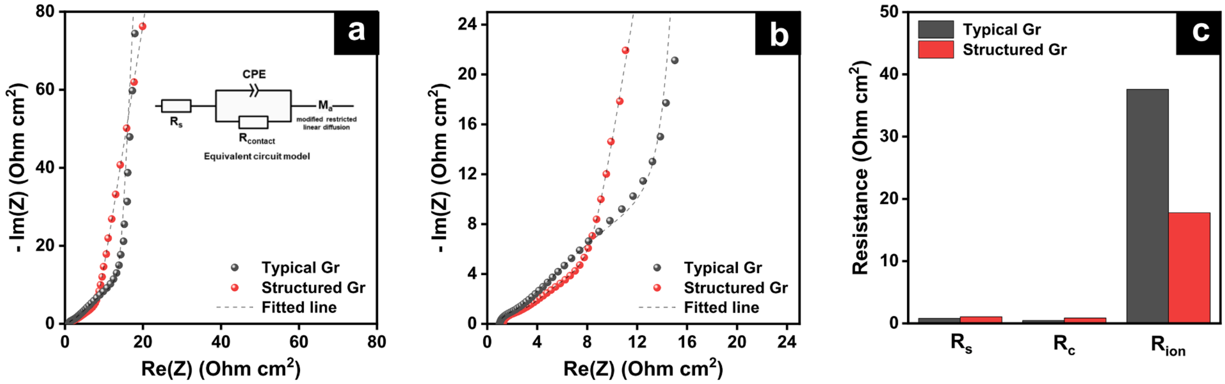

Fig. 6. (a) Nyquist plots of symmetric pristine typical Gr electrodes and structured Gr electrodes. (b) Nyquist plots for closer observation (c) Comparison of each resistance component in typical and structured Gr electrodes.

Table 1
Parameter results of typical and structured Gr.

	Electrode porosity (%)	R_{ion} (Ohm)	Electrode thickness (μm)	Calculated tortuosity
Typical Gr	30	47.87	69	6.67
Structured Gr	50	22.63	91	3.98

surface area of the structured Gr electrode [7].

To confirm the improved kinetic properties obtained by 3-dimensionalization, the rate capability test was conducted on typical and structured Gr electrodes, as shown in Fig. 7(a–c). The discharge capacity of typical and structured Gr at a low current of 0.1C delivers a comparable capacity of approximately 332 mAh g^{-1}. On the contrary, as the current density increased, the discharge capacity of the typical Gr significantly decreased compared to that of the structured Gr. At high

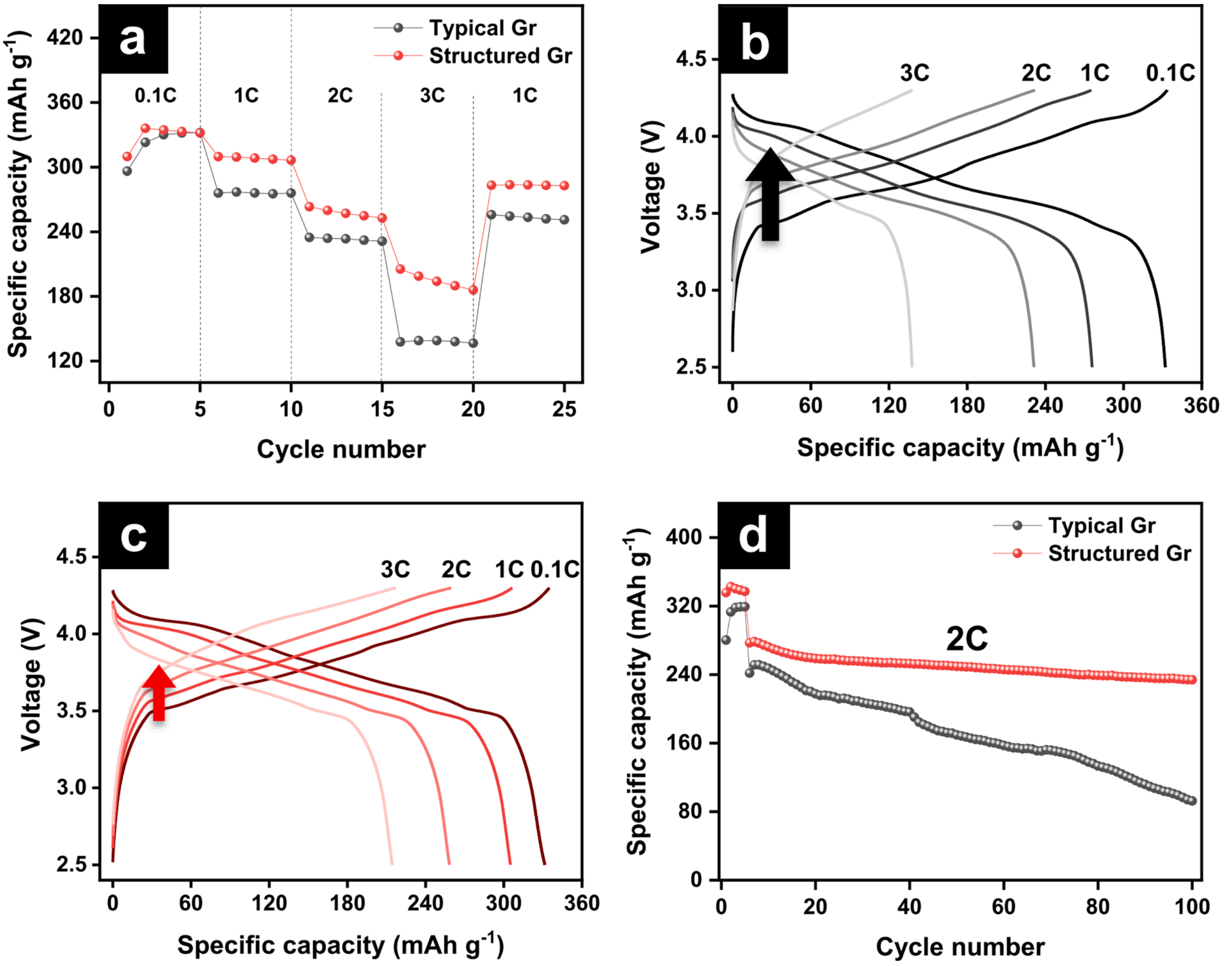

Fig. 7. (a) Rate capability test from 0.1C to 3C after every 5 cycles; charge–discharge curves of (b) typical Gr, and (c) structured Gr at different current rates (d) cycle ability test at 2C.

current rates of 1C, 2C, and 3C, the typical Gr displayed capacities of 276 mAh g^{-1}, 233 mAh g^{-1}, and 138 mAh g^{-1}, respectively, while the structured Gr showed much higher capacities of 308 mAh g^{-1}, 257 mAh g^{-1}, and 194 mAh g^{-1}, respectively. In addition, the charge overpotential of a typical Gr electrode was much higher than that of a structured Gr electrode, especially at high current rates. These results imply that the improved physical properties of pore-structured Gr electrodes affect the electrochemical kinetics owing to the reduced ionic diffusion pathway.

A cycling test was conducted to analyze the effect of a 3D structure on capacity retention at a high current rate of 2C, as shown in Fig. 7d. After 100 cycles at a current rate of 2C, the structured Gr electrode delivered 233 mAh g^{-1}, whereas the typical Gr electrode exhibited 92 mAh g^{-1}, demonstrating that the 3D architecture ameliorated the cycle ability. The enhanced cycle performance is ascribed to the rapid Li^+ ion diffusion in the structured Gr electrode, which prevented ionic concentration polarization that generates a non-homogeneous reaction along the electrode depth [57].

Figure S5 shows the coulombic efficiency (CE) of the Gr electrodes obtained from the results in Fig. 7d. Because a large surface area causes more Li^+ ion consumption during SEI formation [13], a structured Gr electrode shows a lower initial CE (77.3%) than that of a typical Gr electrode (82.6%). On the other hand, during cycling at a current rate of 2C, the structured Gr electrode exhibited a higher CE than that of a typical Gr electrode, demonstrating the prevention of Li metal plating.

To compare the electrochemically active surface area (ECSA) of Gr electrodes, non-aqueous electrochemical double layer capacitance (DLC) was analyzed using CV measurement in Figure S6. Instead of electrolyte containing lithium salts, the non-lithium intercalating electrolyte was used to provide reasonable estimates of ECSA by preventing a faradaic current. Figure S6(a–b) exhibits a semi-rectangular CV scan with a broad current plateau, but the CV curve of a typical Gr electrode shows small curvature at a high scan rate of 8 mV s^{-1} originating from a high tortuous electrode structure [58]. Since a structured Gr electrode delivers a higher C_{sp} value than that of a typical Gr electrode (0.28 F g^{-1} vs. 0.24 F g^{-1}), and capacitance values are proportional to ECSA, it was demonstrated that structured Gr electrodes have larger ECSA.

For further analysis, SEM was applied to post-cycled typical and structured Gr electrodes after 100 cycles at a current rate of 2C. As shown in Fig. 8(a–b), Li metal was plated on the surface of a typical Gr anode, resulting from limiting the Li^+ ion diffusion step. However, the structured Gr electrode in Fig. 8(c–d) maintained its morphology, and no plated Li metal was observed. This is because the interfacial area between the electrolyte and electrode surface layer was enlarged, resulting in an enhanced active site and ionic diffusion rate. The results of the cycle test and SEM in Fig. 7d and Fig. 8(c–d) indicate that pore structuring improves the electrochemical properties and prevents lithium plating, which causes further capacity decay and safety issues resulting from lithium dendrite [59–60].

Table S2 summarizes the cell performance of other studies that facilitate 3D electrode structures. Previous researches deliver significantly enhanced electrochemical properties, demonstrating the effect of physical property on cell performance. Although the laser ablation method shows more significant performance improvement, using

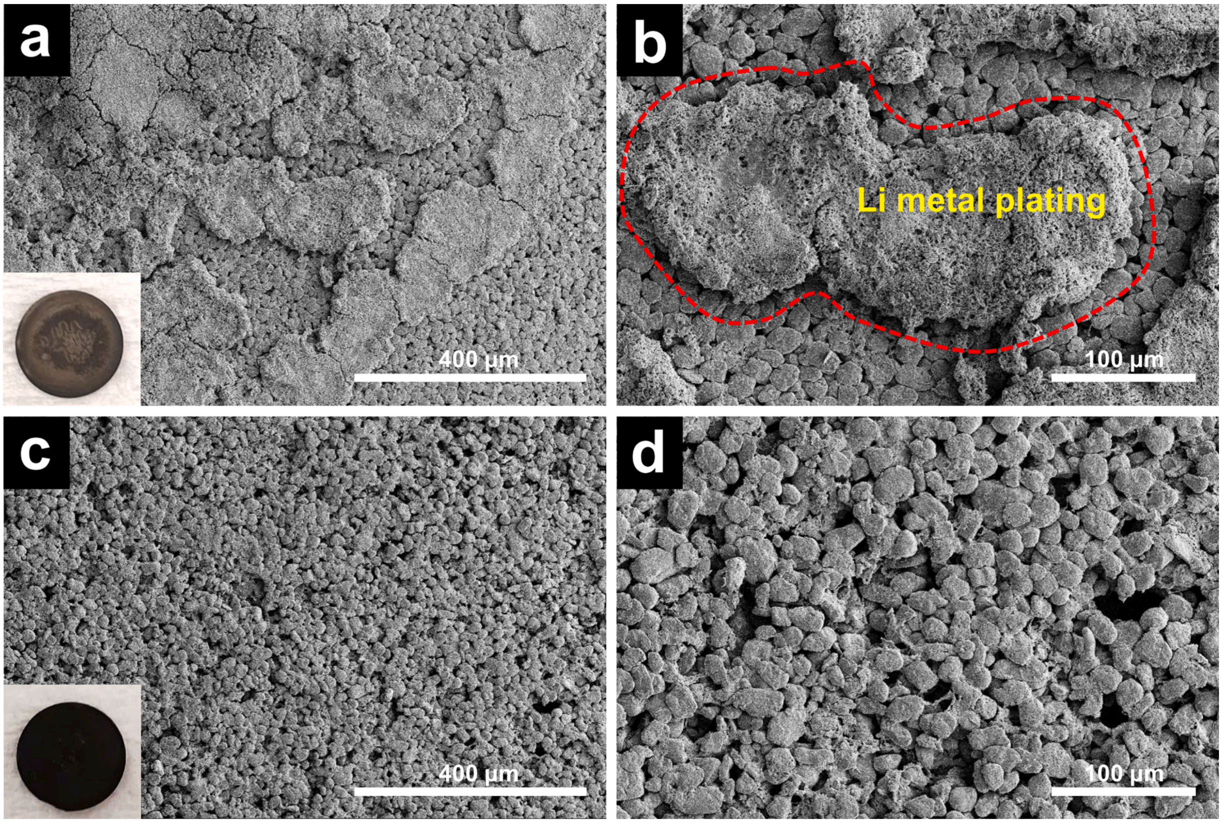

Fig. 8. Top-down SEM images of the (a-b) typical Gr and (c-d) structured Gr electrodes after 100 cycles at 2C (inset images are photographs of post-cycled Gr electrodes).

unzipping polymer method has the advantage of no loss of electrode active material.

4. Conclusion

In this work, we fabricated 3D Gr electrodes using a facile heat-treatment and investigate physico-electrochemical characteristics. The improved physical properties such as high wetting ability, low tortuosity, and large electrode surface area reduce ionic resistance in the structured Gr electrode. As a result, the rate capability of a structured Gr electrode exhibits 194 mAh g^{-1}, whereas a typical electrode shows 138 mAh g^{-1} at a high current rate of 3C. In addition, the structured Gr electrode delivers 2.53 times higher capacity (233 mAh g^{-1}) than a typical Gr electrode (92 mAh g^{-1}) after 100 cycles at a current rate of 2C. Such an enhanced rate and cycle performance are ascribed to 3D electrode structure: micro-sized pores in the structured Gr electrode provide a new electrolyte impregnation route and improve ionic diffusion rate. Since our approach does not require changes to the existing electrode chemistry and slurry process, it is considered one of the most cost-effective and direct-applicable ways to commercial LIBs.

Declaration of Competing interests

The authors declare that they have no known competing financial interests or personal relationships that could have appeared to influence the work reported in this paper.

Acknowledgments

This work was supported by the Korea Institute of Energy Technology Evaluation and Planning (KETEP) and the Ministry of Trade, Industry & Energy (MOTIE) of the Republic of Korea [Grant No. 20204010600340] and a GIST Research Institute (GRI) grant funded by the GIST in 2021.

Supplementary materials

Supplementary material associated with this article can be found, in the online version, at doi:10.1016/j.apsadv.2021.100168.

References

[1] B. Scrosati, J. Garche, Lithium batteries: status, prospects and future, J. power sources 195 (9) (2010) 2419–2430.
[2] F.T. Wagner, B. Lakshmanan, M.F. Mathias, Electrochemistry and the future of the automobile, J. Phys. Chem. Lett. 1 (14) (2010) 2204–2219.
[3] Y. Zuo, et al., Hydrothermal synthesized rugby–like $LiNi_{0.5}Co_{0.2}Mn_{0.3}O_2$ cathode materials with micro-nano structure for high performance Li-ion batteries, J. Electroanal. Chem. 878 (2020), 114660.
[4] D.S. Kim, et al., Surface engineering of graphite anode material with black TiO_{2-x} for fast chargeable lithium ion battery, Electrochim. Acta 258 (2017) 336–342.
[5] D.S. Kim, Y.E. Kim, H.S. Kim, Improved fast charging capability of graphite anodes via amorphous Al_2O_3 coating for high power lithium ion batteries, J. power sources 422 (2019) 18–24.
[6] M. Frankenberger, et al., Laminated Lithium Ion Batteries with improved fast charging capability, J. Electroanal. Chem. 837 (2019) 151–158.
[7] N. Ogihara, Y. Itou, T. Sasaki, Y. Takeuchi, Impedance spectroscopy characterization of porous electrodes under different electrode thickness using a symmetric cell for high-performance lithium-ion batteries, J. Phys. Chem. Lett. 119 (9) (2015) 4612–4619.
[8] X. Lu, et al., 3D microstructure design of lithium-ion battery electrodes assisted by X-ray nano-computed tomography and modelling, Nat. Commun. 11 (1) (2020) 2079.
[9] Y. Zheng, L. Pfäffl, H.J. Seifert, W. Pfleging, Lithium distribution in structured graphite anodes investigated by laser-induced breakdown spectroscopy, Appl. Sci. 9 (20) (2019) 4218.
[10] K. Kitada, et al., Factors determining the packing-limitation of active materials in the composite electrode of lithium-ion batteries, J. Power Sources 301 (2016) 11–17.
[11] A.V. Baskar, et al., Single-step synthesis of 2D mesoporous C_{60}/carbon hybrids for supercapacitor and Li-ion battery applications, Bull. Chem. Soc. Jpn. 94 (1) (2021) 133–140.

[12] A. Azhar, et al., Nanoarchitectonics: a new materials horizon for prussian blue and its analogues, Bull. Chem. Soc. Jpn. 92 (4) (2019) 875–904.

[13] T. Zhang, F. Ran, Design Strategies of 3D carbon-based electrodes for charge/ion transport in lithium ion battery and sodium ion battery, Adv. Funct. Mater. 31 (17) (2021), 2010041.

[14] F. Di, et al., Coral-like porous composite material of silicon and carbon synthesized by using diatomite as self-template and precursor with a good performance as anode of lithium-ions battery, J. Alloys Compd. 854 (2021), 157253.

[15] Z. Li, et al., MoO_x nanoparticles anchored on N-doped porous carbon as Li-ion battery electrode, Chem. Eng. J. 381 (2020), 122588.

[16] W. Pfleging, J. Pröll, A new approach for rapid electrolyte wetting in tape cast electrodes for lithium-ion batteries, J. Mater. Chem. A 2 (36) (2014) 14918–14926.

[17] J. Park, S. Suh, S. Jeong, H.J. Kim, New approach for the high electrochemical performance of silicon anode in lithium-ion battery: a rapid and large surface treatment using a high-energy pulsed laser, J. power sources 491 (2021), 229573.

[18] K.H. Chen, et al., Efficient fast-charging of lithium-ion batteries enabled by laser-patterned three-dimensional graphite anode architectures, J. power sources 471 (2020), 228475.

[19] D. Dang, Y. Wang, S. Gao, Y.T. Cheng, Freeze-dried low-tortuous graphite electrodes with enhanced capacity utilization and rate capability, Carbon N Y 159 (2020) 133–139.

[20] C. Chen, et al., Highly conductive, lightweight, low-tortuosity carbon frameworks as ultrathick 3D current collectors, Adv. Energy Mater. 7 (17) (2017), 1700595.

[21] S. Geier, et al., A wet-chemical route for macroporous inverse opal Ge anodes for lithium ion batteries with high capacity retention, Sustain. Energy Fuels 2 (1) (2018) 85–90.

[22] D.H. Kim, et al., Porosity controlled carbon-based 3D anode for lithium metal batteries by a slurry based process, Chem. Commun. 56 (85) (2020) 13040–13130.

[23] Y.J. Lee, et al., Fabrication of macroporous Si alloy anodes using polystyrene beads for lithium ion batteries, J. Appl. Electrochem. 46 (6) (2016) 695–702.

[24] H.Y. Choi, P. No, Y.J. Lee, J.H. Choi, A pore-structured Si alloy anode using an unzipping polymer for a lithium ion battery, J. Appl. Electrochem. 47 (10) (2017) 1127–1136.

[25] G. Lui, et al., Flexible, three-dimensional ordered macroporous TiO_2 electrode with enhanced electrode-electrolyte interaction in high-power Li-ion batteries, Nano Energy 24 (2016) 72–77.

[26] R. Wang, G. Xu, Y. He, Structure and properties of polytetrafluoroethylene (PTFE) fibers, e-Polymers 17 (3) (2017) 215–220.

[27] W.E. Hanford, R.M. Joyce, Polytetrafluoroethylene, J. Am. Chem. Soc. 68 (10) (1946) 2082–2085.

[28] J. Zhou, L. Xu, L. Li, X. Li, Polytetrafluoroethylene-assisted N/F co-doped hierarchically porous carbon as a high performance electrode for supercapacitors, J. Colloid Interface Sci. 545 (2019) 25–34.

[29] W. Chen, et al., Thermal imidization process of polyimide film: interplay between solvent evaporation and imidization, Polymer (Guildf) 109 (2017) 205–215.

[30] U. Zubair, et al., Lithium polysulfides immobilization exploiting formate-ion doped polyaniline wrapped carbon for Long cycle life sulfur cathodes via conventional electrode processing, Mater. Today Commun. 26 (2021), 101970.

[31] S. An, et al., The state of understanding of the lithium-ion-battery graphite solid electrolyte interphase (SEI) and its relationship to formation cycling, Carbon N Y 105 (2016) 52–76.

[32] M. Frankenberger, et al., SEI Growth impacts of lamination, formation and cycling in lithium ion batteries, Batteries 6 (2) (2020) 21.

[33] E. taer, et al., The relationship of surface area to cell capacitance for monolith carbon electrode from biomass materials for supercapacitor application, J. Phys. Conf. Ser. (2018), 032040, 1116.

[34] Y. Yoon, B. Yan, Y. Surendranath, Suppressing ion transfer enables versatile measurements of electrochemical surface area for intrinsic activity comparisons, J. Am. Chem. Soc. 140 (7) (2018) 2397–2400.

[35] E.N. Primo, et al., Understanding the calendering processability of Li $(Ni_{0.33}Mn_{0.33}Co_{0.33})O_2$-based cathodes, J. power sources 488 (2021), 229361.

[36] M. Singh, J. Kaiser, H. Hahn, A systematic study of thick electrodes for high energy lithium ion batteries, J. Electroanal. Chem. 782 (2016) 245–249.

[37] J. Hu, et al., Evolution of the rate-limiting step: from thin film to thick Ni-rich cathodes, J. power sources 454 (2020), 227966.

[38] H.H. Park, H.J. Kim, Diphenyl Diselenide as SEI-forming Additive for a High-voltage $LiCoO_2$/Graphite Battery, J. Electrochem. Soc. 167 (7) (2020), 070555.

[39] T.G. Woo, et al., Effect of N_2 plasma treatment on the adhesion of Cu/Ni thin film to polyimide, Met. Mater. Int. 17 (5) (2011) 789–795.

[40] X.L. Zhu, et al., Analysis by using X-ray photoelectron spectroscopy for polymethyl methacrylate and polytetrafluoroethylene etched by KrF excimer laser, Surf. Sci. Spectra 253 (6) (2007) 3122–3126.

[41] C. Girardeaux, J.J. Pireaux, Analysis of poly (tetrafluoroethylene)(PTFE) by XPS, Surf. Sci. Spectra 4 (2) (1996) 138–141.

[42] M.Bin B. Ahmad, et al., Preparation, characterization and thermal degradation of polyimide (4-APS/BTDA)/SiO_2 composite films, Int. J. Mol. Sci. 13 (4) (2012) 4860–4872.

[43] M.Bin B. Ahmad, et al., Comparison of in situ polymerization and solution-dispersion techniques in the preparation of polyimide/montmorillonite(MMT) nanocomposites, Int. J. Mol. Sci. 12 (2011) 6040–6050.

[44] D. Yao, Y. Yang, Y. Deng, C. Wang, Flexible polyimides through one-pot synthesis as water-soluble binders for silicon anodes in lithium ion batteries, J. power sources 379 (2018) 26–32.

[45] W. Chen, et al., Thermal imidization process of polyimide film: interplay between solvent evaporation and imidization, Polymer (Guildf) 109 (2017) 205–215.

[46] J. He, L. Zhang, Polyvinyl alcohol grafted poly (acrylic acid) as water-soluble binder with enhanced adhesion capability and electrochemical performances for Si anode, J. Alloys Compd. 763 (2018) 228–240.

[47] G. Zhang, et al., Enhancement in liberation of electrode materials derived from spent lithium-ion battery by pyrolysis, J. Clean. Prod. 199 (2018) 62–68.

[48] J.S. Kim, et al., Effect of polyimide binder on electrochemical characteristics of surface-modified silicon anode for lithium ion batteries, J. power sources 244 (2013) 521–526.

[49] S. Uchida, M. Mihashi, M. Yamagata, M. Ishikawa, Electrochemical properties of non-nano-silicon negative electrodes prepared with a polyimide binder, J. power sources 273 (2015) 118–122.

[50] H. Zheng, L. Tan, G. Liu, X. Song, V.S. Battaglia, Calendering effects on the physical and electrochemical properties of $Li[Ni_{1/3}Mn_{1/3}Co_{1/3}]O_2$ cathode, J. Power Sources 208 (2012) 52–57.

[51] N. Ogihara, Y. Itou, S. Kawauchi, Ion transport in porous electrodes obtained by impedance using a symmetric cell with predictable low-temperature battery performance, J. Phys. Chem. Lett. 10 (2019) 5013–5018.

[52] D.A.G. Bruggeman, Berechnung verschiedener physikalischer Konstanten von heterogenen Substanzen. I. Dielektrizitätskonstanten und Leitfähigkeiten der Mischkörper aus isotropen Substanzen, Ann. Phys. 416 (7) (1935) 636–664.

[53] F. Pouraghajan, et al., Quantifying Tortuosity of Porous Li-Ion Battery Electrodes: comparing Polarization-Interrupt and Blocking-Electrolyte Methods, J. Electrochem. Soc. 165 (2018) A2644.

[54] J. Landesfeind, et al., Tortuosity of Battery Electrodes: validation of Impedance-Derived Values and Critical Comparison with 3D Tomography, J. Electrochem. Soc. 165 (2018) A469–A476.

[55] L. Li, et al., Fabrication of Low-Tortuosity Ultrahigh-Area-Capacity Battery Electrodes through Magnetic Alignment of Emulsion-Based Slurries, Adv. Energy Mater. 9 (2) (2019), 1802472.

[56] T. Anwar, et al., Titania nanotube array decorated in polymer matrix as a free-standing anode material for lithium-ion batteries, Mater. Today Commun. (2020), 101760.

[57] K.Y. Park, et al., Understanding capacity fading mechanism of thick electrodes for lithium-ion rechargeable batteries, J. power sources 468 (2020), 228369.

[58] L.S. Rodionova, B.K. Filanovskii, M.L. Petrov, Electrolytic conductivity of potassium 2-phenylethyneselenolate in tetrahydrofuran and acetonitrile, Russian J. General Chem. 71 (1) (2001) 85–88.

[59] Q. Lv, et al., Three-dimensional nitrogen-doped graphene aerogel toward dendrite-free lithium-metal anode, Ionics (Kiel) 26 (1) (2020) 13–22.

[60] S.B. Son, et al., Fast charge-driven li plating on anode and structural degradation of cathode, J. Electrochem. Soc. 167 (14) (2020), 140506.